Chapter 7. UWB Signal processing

7.1. Introduction

In the last chapter of this work, we discuss some signal processing techniques used on GPR data. Until now we only have treated hardware aspects of the UWB GPR and we have modelled the system in the time domain. The question is if we can use this additional information on the hardware of the system for adapting or developing signal processing algorithms.

Further there is the question if the UWB approach in the demining application yields the necessary advantages over the conventional GPR. Many authors suggest that there is a lot of information in the early- and especially in the late-time response (also called the resonant part) of buried objects to short transient pulses. This information could be very useful for the classification of targets. The verification of this statement however is not straightforward. In the previous chapter we saw that UWB GPR was able to detect shallow buried mines. But despite the better depth resolution and the fact that the backscattered signal contains more frequency information on the target, the visual classification of objects in the B- or C-scans is not feasible. In this chapter, we will report some conclusions concerning the use of signal processing techniques that are more adapted to UWB signals.

Signal processing on the raw data coming from a conventional GPR has mainly two objectives. First it can be used to reduce the clutter. Clutter can be defined as

backscattered signals that are not from possible targets, but occur in the same time window and have similar spectral characteristics. In GPR applications some examples of clutter sources are the air-ground interface, multiple reflections between antenna and ground, reflections from side-lobes and discontinuities in the ground like stones and roots. Unlike conventional radar systems, the targets and clutter sources are both static, so clutter removal techniques like moving target indicator (MTI) can't be used. In the scope of the HUDEM project, work has been done in the domain of clutter reduction on UWB data [1].

A second objective of the signal processing is in general to enhance the quality of the images, so that the interpretation by a human operator becomes easier and more correct. Noise reduction methods [2] as well as focussing techniques to reduce the influence of the antenna beamwidth, called migration techniques, belong to this class of signal processing techniques.

Another way of classifying the signal processing algorithms is by the type of signals to which they are applied. Signal processing techniques can be applied to A-scans, B-scans or C-scans. In the next section a brief overview of a few basic signal processing techniques on A-scans will be given. The overview is far from complete, only the techniques, used or developed in the scope of this work, are restrained. Furthermore we report on two well-known signal processing techniques on A-scans that are more adapted to UWB signals and discuss briefly their target classification capability, without addressing the problem of classification itself. In the following section, an overview of migration techniques is given. This section must be seen as an introduction to the last section of this chapter where a fast and computational not intensive migration technique is described. The novelty of the algorithm is that the characteristics of the GPR system and the ground are taken into account in the algorithm. This is normally not the case in the conventional migration techniques.

7.2. A-scans processing

7.2.1. Overview of A-scan processing

DC offset removal

From the physical point of view, the mean value of an A-scan has to be zero or close to zero. Many receivers however have a DC offset that is different from zero and eventually slowly drifting as a function of time. Therefore it is advised to compensate for this offset. In the assumption that the offset stays constant over the time duration of the A-scan, it can be removed by

$$a'(n) = a(n) - \frac{1}{N}\sum_{i=0}^{N-1} a(i) \qquad \text{for} \quad n: 0 \rightarrow N-1 \qquad \textbf{(7. 1)}$$

where

$a(n)$ is the raw A-scan,

$a'(n)$ the A-scan after DC offset removal,

n the sample number of the A-scan, and

N the total number of samples per A-scan.

Background subtraction

In many GPR data, there is clutter present that always appears at the same time in an A-scan or in a series of neighbouring A-scans. Examples of this kind of clutter are a flat air-ground interface, a horizontal layer in the ground, or antenna ringing. These clutter sources create horizontal lines in the B- or C-scans and can in some cases obscure a target. The reduction of this kind of clutter can be achieved by subtracting from each A-scan the average of a number of neighbouring A-scans or even the average of all the A-scans in a B-scan. The algorithm is mathematically described as

$$a_i'(n) = a_i(n) - \frac{1}{K}\sum_{k=0}^{K-1} a_k(n) \qquad \textbf{(7. 2)}$$

where

$a_i(n)$ is the i^{th} A-scan in the raw data,

$a_i'(n)$ the i^{th} A-scan of the processed data,

K the number of A-scans to be averaged before subtraction. In general, the neighbouring A-scans are taken symmetrically around the A-scan that is processed.

If the clutter is present in the whole B-scan, the number K is often taken equal to the total number of A-scans in the B-scan, so that the average of the whole B-scan is subtracted from each individual A-scan.

Note that other mathematical operations than the average, as for instance the median, are also possible and sometimes lead to better results.

Care has to be taken with the background subtraction, as it can create artefacts in the image and sometimes inversion in the intensity of the A-scans, leading to an inversion of the colour in the B-scan. Fig. 7-1 shows a B-scan of a Belgian AP mine, type PRB-409, buried at a depth of 5 cm in loam. The PRB-409 is a very flat and difficult to detect AP mine. In the unprocessed image on the left, the antenna coupling and the air-ground interface is clearly visible. In the processed image at the right, the little AP mine becomes more visible. In this example, the average of the whole B-scan is taken to be subtracted from each individual A-scan.

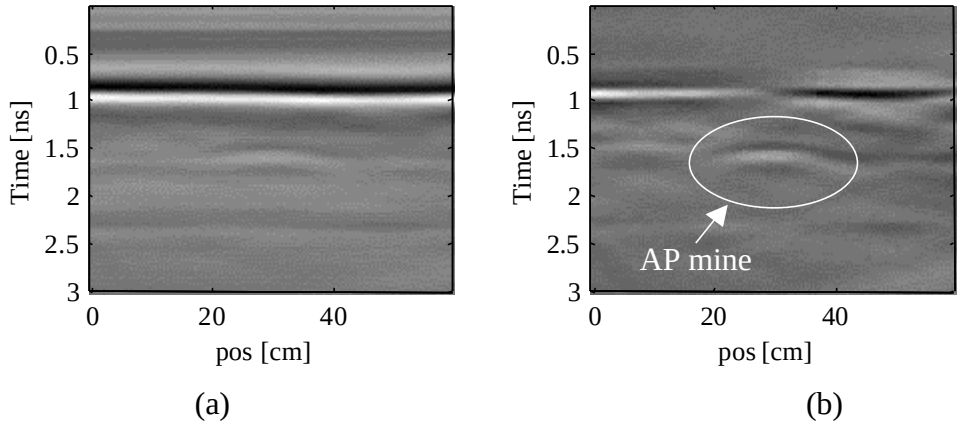

(a) (b)

Fig. 7-1: B-scan of a PRB-409 AP mine (a) before and (b) after background subtraction

Time-varying gain

As already mentioned in Chapter 2, the received signal is attenuated by the losses in the ground and by the spreading losses. The later in time the reflection appears in an A-scan, the further it has travelled in the ground, hence the more it was attenuated by the above mentioned losses. This can be compensated for by applying a time-varying gain. As our receiver had no such gain implemented in hardware, it can also be done software wise. The disadvantage of this approach however is that the noise and clutter in the A-scan are also amplified, therefore we will almost never apply this signal processing technique to our data.

Extraction of the scattering centres

In radar applications, it is well known that the backscattering from a complex target can be approximately modelled by a discrete set of scattering centres. A method to extract the scattering centres of the target, and thereby enhancing depth resolution, is by deconvolving the signal source and antenna IR from the backscattered signal. Due to the band limited nature of the emitted wave and the effects of noise, deconvolution of the signal source and antenna IR is an ill-posed problem. Furthermore with the deconvolution one cannot take into account the dispersive behaviour of the ground.

Indeed, an additional problem to extract the scattering centres in an A-scan is the broadening of the reflected signal due to the dispersive behaviour of the ground. An often-used deconvolution technique is the *Wiener filter* or a variant of this filter. More details about the Wiener filter can be found in Section 7.4. A disadvantage of this filter is that the noise spectral density and the signal spectral density must be known.

In this section we present a processing technique for extracting the scattering centres, which is more robust to noise and can partially compensate for the dispersive behaviour of the ground [3][4]. The method is based on the Continuous Wavelet Transformation (CWT) [5] and uses the dilatation properties of the wavelets to counteract the dispersive behaviour of the ground. The knowledge of the exact source signal and the antenna IR is basic in this method.

For clarity reasons let us summarise a somewhat simplified version of the time domain radar range equation (5.13). The received voltage due to a reflection on one buried object can be described by

$$V_{rec}(t) = K\, g_d(t) \otimes h_{N,Tx}(t) \otimes \Lambda(t) \otimes h_{N,Rx}(t) \otimes \frac{dVs(t)}{dt} \qquad \textbf{(7. 3)}$$

where

K is a constant taking into account the spreading loss, the transmission coefficients, the off boresight position of the target, etc.,

$h_{N,Tx}(t)$ is the normalised impulse response of the transmitting antenna on boresight,

$h_{N,Rx}(t)$ the normalised impulse response of the receiving antenna on boresight,

$g_d(t)$ the impulse response representing the two-way path length loss in the ground,

$\Lambda(t)$ the impulse response of the buried target, and

V_S the excitation voltage at the antenna feed.

If more than one target is present in a scene and the targets are considered to be independent of each other, the total received voltage at the receiver can then be written as a sum of the received voltages of each individual (and independent) target.

Furthermore, in this method we assume that if k scattering centres approximately model a scenario of complex targets and planner interfaces, then the received A-scan can always be written as a sum of *k* individual normalised wavelets:

$$a(t) \approx \sum_{p=1}^{k} B_p h_{a_p,t_p}(t) \qquad \textbf{(7. 4)}$$

where $h_{a_p,t_p}(t)$ represents the backscattered wavelet on scattering centre *p* and B_p its amplitude. According to the time domain radar range equation (7.3), and neglecting for the moment the influence of the ground, the backscattered wavelet $h_{a_p,t_p}(t)$ must have the shape of

$$h_{N,Tx}(t) \otimes h_{N,Rx}(t) \otimes \frac{dV_S(t)}{dt} \qquad \textbf{(7. 5)}$$

In the case of the laboratory UWB GPR, expression (7.5) resembles a derivative of a Gaussian pulse. To extract these individual wavelets from $a(t)$, the Continuous Wavelet Transformation (CWT) is used. The CWT is a time-frequency analysis technique that gives in a time-scale plane the correspondence between a time signal $a(t)$ and a basic wavelet $h_{a_p,t_p}(t)$, delayed by t and scaled by a dilatation coefficient a. The basic wavelet for this transformation is chosen to fit the shape of expression (7.5). Normalising the energy in the wavelet, results in the basic wavelet

$$h_{a_p,t_p}(t) = \frac{1}{\sqrt{a_p}} \sqrt{\frac{2}{\sqrt{p}}} \left(\frac{t - t_p}{a_p} \right) e^{-\frac{1}{2}\left(\frac{t-t_p}{a_p}\right)^2} \qquad \textbf{(7. 6)}$$

The delay t_p takes into account the two-way travelling time between the antennas and the scattering centre p. The dilatation coefficient a_p scales the wavelet and thereby partially compensates for the broadening of the reflection on the scattering centre due to the dispersive behaviour of the ground. The coefficients B_p are found one at a time by an iterative procedure. One begins at stage *p=1*. The CWT of received signal is computed, using (7.6) as basic wavelet. The parameter B_1 is found as the maximum wavelet coefficient of the transformations, with a_1 and t_1 as corresponding dilatation coefficient and time-delay of the wavelet. Then $B_1 h_{a_1,t_1}(t)$ is subtracted from the received signal. This procedure is iterated to generate as many coefficients as needed to accurately represent the original received signal. Fig. 7-2 shows the result of this method on an A-scan, representing a PMN mine in loam at 5 cm of depth. In this example only five scattering centres are calculated.

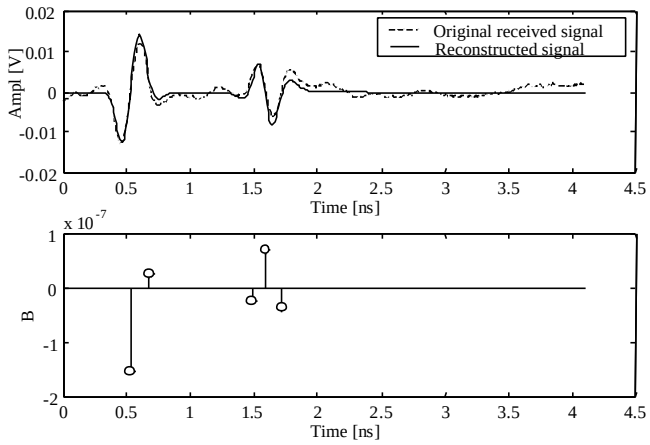

Fig. 7-2: (upper) Approximation of A-scan as a sum of normalised wavelets, (lower) coefficients B_p of the five scattering centres

The lower plot of Fig. 7-2 can be seen as the deconvolved version of the solid curve in the upper plot of Fig. 7-2. The first two scattering centres in the lower plot of Fig. 7-2 represent the reflection on the air-ground interface, the last three scattering centres represent the reflection on the object.

In [6] it is suggested that the scattering centres of an object are characteristic of that object. Hence the last three scattering centres in the lower plot of Fig. 7-2 can be used

as a template to look for similar objects (in this case PMN mines) in other A-scans. A more detailed study on the data coming from the UWB GPR revealed that the template of an object indeed does not alter too much as a function of the depth of the object [3]. However, the relative amplitude of the scattering centres, the time interval between the scattering centres and even the number of scattering centres is very sensitive to variations in inclination of the object and to variations in the surrounding media of the objects. Furthermore, once the energy in the reflection on the target becomes too small, because the target is too deep or the attenuation in the ground too high, the retrieval of a stable template is almost impossible. As a whole the method was not found robust enough to retrieve reliable features for classification algorithms for buried objects on our data.

A possible application of this processing technique for extracting the scattering centres is to use it as a method to reduce the amount of data. A problem often encountered when working with C-scans is that the amount of data becomes too large. A way of reducing this amount of data is to only store the information on the scattering centres per A-scan. It is seen that in most of the cases an A-scan is accurately represented by a sum of 5 wavelets. Each wavelet is characterised by one triplet (B_p, t_p, a_p). This means that for an A-scan of 512 points, only 15 values have to be stored instead of 512, hence a data reduction of 1/34. The complete A-scan can always be reconstructed from those 15 values. The extraction of the scattering centres is very fast and can easily be implemented in real time. A decomposition of an A-scan of 512 points in a sum of 5 wavelets takes only 0.39 sec in MatLab code on a PC.

Fig. 7-3 shows a 3D plot of a C-scan of a buried mine by only representing the scattering centres of each A-scan. The amplitudes of the coefficients B_p of the scattering centres are represented by colours.

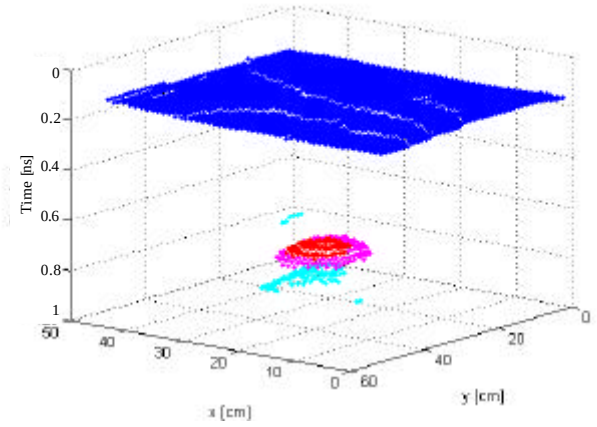

Fig. 7-3: 3D plot of a C-scan by only representing the scattering centres

7.2.2. UWB signal processing on A-scans

In Chapter 5 we mentioned that the response of an object on a fast transient impulse can be split into two parts: the early time response and the late time response. The late time response is considered to begin after a time interval, which is of the order of the wave transit time though the object. The late-time response (also called the resonant part) is governed by the complex natural resonances of the object. These complex natural resonances are supposed to be independent of the orientation of the object, and contain valuable information for target recognition and clutter reduction.

Pole extraction

A technique for extracting the natural resonance frequencies of the late-time transient response, is given by Prony-type methods. In Prony-type methods it is assumed that the late-time response of a target can be modelled as an all-pole system, and hence can be written as a summation of complex exponentials:

$$y(n) = \sum_{i=1}^{p} D_i e^{s_i nT} \qquad \textbf{(7. 7)}$$

where

$y(n)$ is a vector (sequence) of equally spaced data points,

N the total number of data points,

T the sampling period,

s_i the i^{th} complex pole,

D_i the residue of the i^{th} complex pole, and

p the total number of poles.

In 1795 Prony gave a method of solution for finding the complex poles to fit a vector of equally spaced data points with length $N = 2p$ [7]. This method however performs poorly in the presence of noise [8]. To overcome the problem, improved Prony-type methods have been developed. Equation (7.7) can be written as a recursive differential equation

$$y(n) = -\sum_{k=1}^{p} a(k)y(n-k) \qquad for\, n \geq p \qquad \textbf{(7. 8)}$$

This auto-regressive recurrence equation, also called the forward linear prediction equation can be written for the different measured data points

$$\begin{bmatrix} y(p) & y(p-1) & \cdots & y(1) \\ y(p+1) & y(p) & \cdots & y(2) \\ \vdots & \vdots & \ddots & \vdots \\ y(N-1) & y(N-2) & \cdots & y(N-p) \end{bmatrix} \begin{bmatrix} a(1) \\ a(2) \\ \vdots \\ a(p) \end{bmatrix} = -\begin{bmatrix} y(p+1) \\ y(p+2) \\ \vdots \\ y(N) \end{bmatrix} \qquad \textbf{(7. 9)}$$

or in short

$$Ya = h$$

The matrix Y is called the data matrix and the vector h is called the observation vector. The unknown complex amplitude vector a can be calculated by solving the

linear prediction equation (7.9) for $N > 2p$ in the sense of least squares [9]. Once the amplitude vector a has been found, the complex poles of the system can be calculated as the zeros of the polynomial

$$1 + a(1)z^{-1} + a(2)z^{-2} + ... + a(p)z^{-p} \qquad \textbf{(7. 10)}$$

The residues D_i can be found by solving using equation (7.7) in the sense of the least squares. The same can be done using the backward linear prediction equation or a combination of both [9]. Other improved prony-type methods based on linear prediction are found in [10][11].

Another problem besides the measurement noise is the lack of *a priori* knowledge on the exact number of poles of the system, *i.e.* the order $M = p$ of the system. In [12][13], the estimation of M is done based on the singular value decomposition (SVD) of the data matrix Y. If no noise is present in the data, the rank of Y will be equal to M and only M eigenvalues will be found different from 0. In our study, we implemented the Total Least Square method (TLS) [13]. In this approach the noise in the data matrix and the observation vector is reduced simultaneously. The number of poles will be estimated by use of the SVD of the augmented matrix $[Y \mid h]$; only the poles with a sufficiently high energy are kept.

In an experimental study [3], the TLS method is tested on the backscattered signals of metal discs and of different types of AP mines. The aim of the study was to verify if the location of the poles is characteristic for an object, and if the location can be used for the classification or even recognition of that object. The study showed that the location of the poles is not stable and this for mainly two reasons. The first reason is the large damping of the resonances. AP mines are so called low-Q targets, *i.e.* targets with a large damping factor. This damping factor is related to the target shape, the dielectric contrast and the surrounding medium [14]. As a consequence the usable length of the data vector $y(n)$ becomes shorter and the results from the TLS method become highly unstable. A second problem is related to the choice of the starting point of the data vector $y(n)$. In theory Prony-type methods must be applied only on

the late time response, as the early time response is a function of the orientation of the object. AP mines however are relatively small compared to the duration of the incoming pulse that is used, hence the end of the early time response interferes with the beginning of the late time response. Indeed, we observed that in practice it is almost impossible to separate the early time response from the late time response and that the position of the poles found by the TLS method is very sensitive to changes of the starting point of the data vector. As a whole we concluded that the results of the pole extraction algorithm are not robust enough to be used for the classification of AP mines in practical applications.

Time-frequency analysis

Time-frequency analysis is a well adapted signal processing technique for analysing non-stationary data and has recently been applied with success to electromagnetic UWB scattering data [15][16]. A problem encountered with the spectrum analysis of a signal using a Fourier transform is that the signal is supposed to be stationary. With the data coming from an UWB GPR, this assumption is not true. The non-stationary character of the data in an A-scan makes that time-frequency analysis techniques like Short-Time Fourier Transform (STFT) and Continuous Wavelet Transformations (CWT) would perform better than the conventional Fourier transformations. These techniques give a spectrum analysis that is more localised in time, hence they are good candidates for the analysis of the late time response of targets.

The Short-Time Fourier Transform (STFT) is a technique where a sliding window (often a Gaussian window) is applied to the data in order to limit the signal in time. A Fourier Transform is then performed on the windowed data for each position of the window. The STFT on a time signal $x(t)$ results in a two dimension function, time *versus* frequency, and is expressed as

$$G(t,w) = \frac{1}{\sqrt{2p}\,s} \int_{-\infty}^{+\infty} x(t)\, e^{-(t-t)^2/2s^2}\, e^{jwt}\, dt \qquad \textbf{(7. 11)}$$

where t is the centre of the sliding Gaussian window and s the standard deviation.

The Continuous Wavelet Transformations (CWT) is a technique where the time signal $x(t)$ is decomposed into a continuous set of wavelets, which are derived from a basic wavelet by expansion (contraction) and shifting in time. The CWT is expressed as

$$W(t,a) = \frac{1}{\sqrt{|a|}} \int_{-\infty}^{+\infty} x(t)\, h\left(\frac{t-t}{a}\right) dt \qquad \textbf{(7. 12)}$$

where $h(t)$ is the basic wavelet (also called the mother wavelet), t is the time shift of the wavelet and a the scale factor. The result of a CWT on an A-scan gives a two dimensional representation of the signal, time *versus* scale-factor. In analogy with the power spectrum representation of a Fourier transformation, a CWT is often represented in what is termed a scalogram, defined as

$$SCAL_W(t,a) = |W(t,a)|^2 \qquad \textbf{(7. 13)}$$

An important point in CWT is the choice of the mother wavelet [16]. For seismic applications the Morlet wavelet is often used [5]. In our research, we also used the Morlet wavelet and tested it on the data coming from the UWB GPR [17]. Although CWT could give an indication of the presence of a target, the results of CWT with respect to the classification of objects was found to be limited, probably because of the same reasons as mentioned in the paragraph on pole extraction.

Fig. 7-4 shows two scalograms: one of an A-scan with only a reflection on the air-ground interface, and one of an A-scan with a target present.

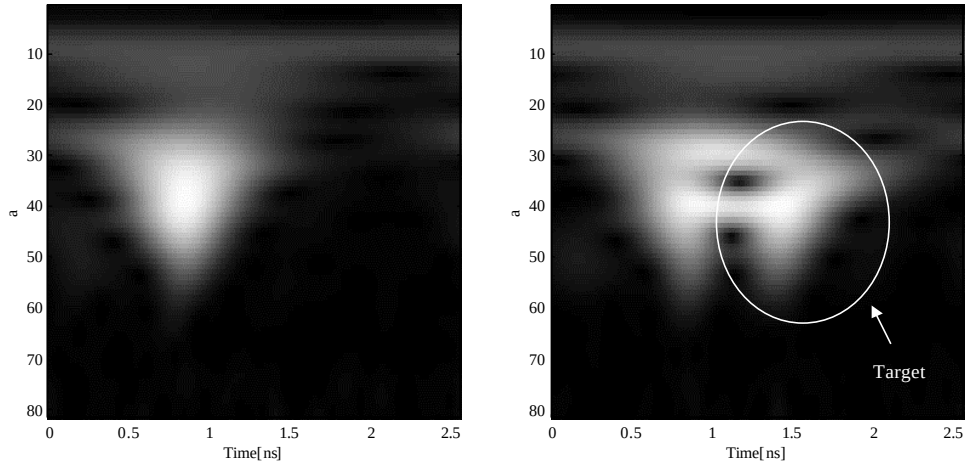

(a) (b)

Fig. 7-4 : (a) Scalogram of an A-scan without target, (b) scalogram of an A-scan with target

The study of UWB signal processing techniques on A-scans coming from the UWB GPR was mainly experimental. The first conclusions drawn from this study were not promising enough for us to continue research in this direction. From this point, an important reorientation of the work in the domain of signal processing was done. Until now we hoped to find sufficient information on the target in an A-scan, because the UWB GPR could then be used in the same way as a metal detector, *i.e.* producing an alarm when a mine or a mine-like target is detected. Considering our rather disappointing experience with the UWB signal processing techniques on A-scans, we decided to concentrate our work more on the interpretation of C-scans, to retrieve information on the shape and dimensions of the buried target.

7.3. Migration

7.3.1. General

The data coming from a GPR, even after optimal A-scan processing will still be unfocussed. Because of the beam-width of the transmitting and receiving antenna, the reflections on a structure will be smeared out over a broad region in the recorded data.

The family of processing algorithms that try to reconstruct, from the recorded B- or C-scans at the surface, the reflecting structure present in the sub-surface, is called *migration*. The aim of migration techniques is to focus reflections in the recorded data back into the true position and physical shape of the target. In this respect, migration can be seen as a form of spatial deconvolution that increases spatial resolution.

The migration techniques received much attention in the last 30 years in seismic and geophysical engineering. The first migration methods were geometric approaches. After the introduction of the computer, more complex techniques, based on the scalar wave equation, were introduced. A good overview of these techniques is given in [18] and [19].

Migration techniques applied on GPR images are sometimes called 1D-SAR imaging techniques. Indeed, migration uses data coming from different antenna position and increases azimuth (cross range) resolution. In this perspective the name 1D-SAR technique is correctly chosen. Note that SAR techniques used in radar usually make more approximations than the migration techniques in seismic. In seismic most of the migration algorithms are based on a backpropagation (inverse extrapolation) of the wave field, described by a scalar wave equation. Until the late 1980s, SAR techniques were based on differences in travel time (or phase) and used plane wave approximations. It is only recently that processing techniques, similar to migration algorithms in seismic, are used in synthetic aperture radars [20].

In Section 7.3.3 some existing migration techniques, applicable on GPR data, will be introduced. Although most of the techniques are originally developed for acoustic sounding, using scalar pressure-wave propagation theory, they are applied with success to electromagnetic sounding. In electromagnetic sounding the fields have a vectorial character and hence the scalar seismic processing algorithms can in theory not be used. In practice however, as most GPRs only radiate and measure one scalar component of the EM field, the seismic migration techniques for scalar fields perform well. In this chapter, to simplify the analysis, we will also make this approximation and replace the vector field by a scalar one. Another difference between electromagnetic and acoustic sounding is the way in which the data are recorded. In the GPR case, the distance between the transmitting antenna and the receiving antenna

is always constant. In seismic terminology, this is called constant-offset data. If the distance between the two antennas is negligible, this is called zero-offset data. Further, with the laboratory UWB GPR, the antennas are used off the ground. This means that the migration algorithm must be modified to take into account the different velocities of the two media (air and ground) and the diffraction on the air-ground interface. If possible, we will suggest such a modification. More mathematical details on the migration algorithm are found in Appendix B.

7.3.2. Exploding source model

A model often used in seismics to explain the mathematics behind some of the methods, is the model of the exploding source. We present the model here because it allows some definitions of terms and illustrates well the migration problem. The geometry of the model is represented on Fig. 7-5. The exploding source is located in the xz-plane, denoted the *object plane*. At time $t = 0$, the sources in the object plane explode and send out waves. The waves propagate as a function of time, represented on a horizontal axis, and reach the surface. The receivers, located along the x-axis, at $z = 0$, record the data. The plane in which the data is recorded is defined as the *data plane*. The recorded data are denoted $b(x, z = 0, t)$ or in short $b(x, t)$.

The ideal migration method transforms the data $b(x, z = 0, t)$ from the data plane back into the object plane $b(x, z, t = 0)$. Due to a number of unknowns, the reduced data set, the complexity of the subsurface and the noise present in the data, a complete inversion is difficult and computational intensive. In many cases it is even impossible, or can lead to unreliable results. All migration algorithms are based on a linearisation of the wave scattering problem. This means that the interaction of the field inside the scatterer and between different scatterers present in the scene is neglected. This approximation is known from optics as the Born approximation [21]. The result of the migration method on the recorded data is called the migrated image $\hat{O}(x, z)$. The migrated image is an estimation of the object plane. Sometimes the migrated image is not represented as a function of the depth z, but as a function of time. One reason for this is that the estimation of the propagation velocity in the subsurface is limited in

accuracy. The migration process resulting in the data $\hat{O}(x,t)$ is then called *time migration.* If the propagation velocity of the medium is known, there is a direct relation between the time and the depth.

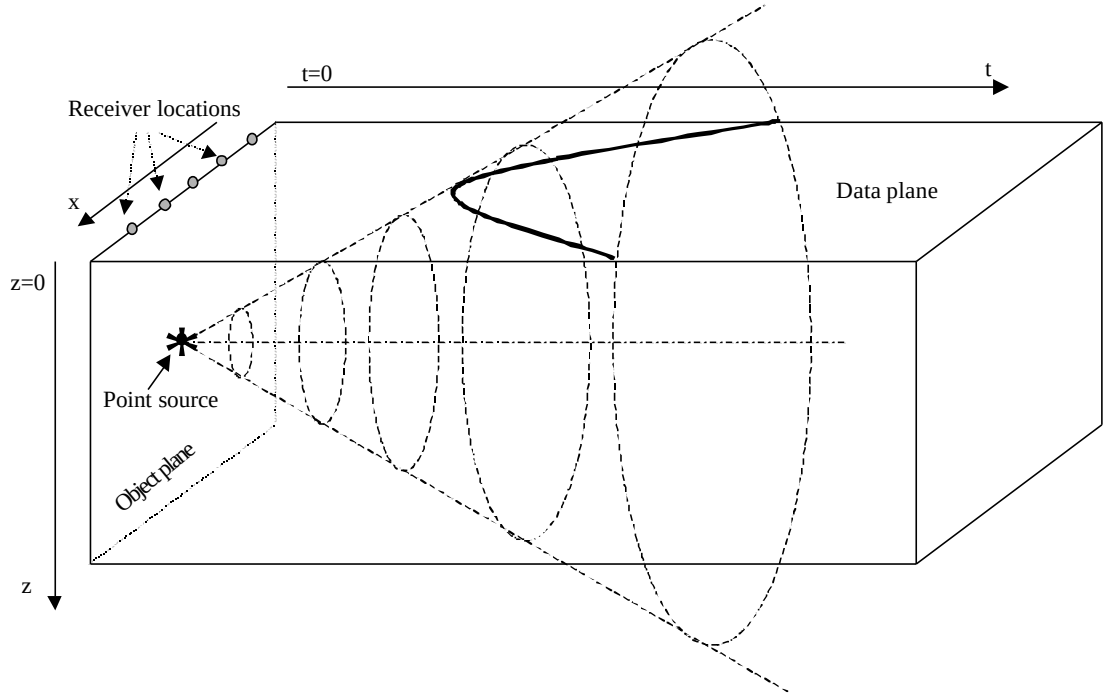

Fig. 7-5: The geometry of the exploding sources model

The data, resulting from an exploding source model is largely equivalent with the zero-offset data of a GPR, with one important distinction. The zero-offset data is recorded as two-way travelling time, while the data from the exploding source model represents the one-way travelling time. To make the data comparable, one can always imagine that the velocity of propagation is half the value of the actual medium velocity in the exploding source model.

Note that the notions *data-* and *object planes* are represented here as 2D planes. This will only be the case if B-scans are recorded. For C-scans, the dimension of the data increases by one, and the two planes have to be considered as volumes.

Further we assume that the propagation velocity in the ground remains constant with depth and that we only want to migrate the top region of the recorded data down to a depth of 20 cm. These two assumptions introduce some simplifications in a lot of the

methods. An extension to a variable propagation velocity in depth and even cross-range is not possible in all of the methods.

7.3.3. Overview of existing migration methods

Diffraction-summation

The first technique is a relatively straightforward method, but it illustrates well the general principle of migration. Consider a 3D data set $b(x,y,t)$ recorded in the data plane. Each point in the migrated image $\hat{O}(x,y,z)$ is the result of a summation of the recorded amplitudes in the data-plane along a diffraction hyperbola, whose curvature is governed by the medium velocity and the depth of the point to be migrated. If there is an object in the apex of the diffraction hyperbola, the amplitudes will add. If not, the summation of the non-coherent data along the diffraction hyperbola tends to zero.

Suppose the data $b(x,y,t)$ is recorded with a monostatic GPR by moving the antennas on the ground in the xy-plane, taking a measurement $b(x_j,y_k,t)$ at position $(x_j,y_k,0)$, with $j=1,2,..,J$ and $k=1,2,..,K$. The migrated image $\hat{O}(x,y,z)$ is then calculated by

$$\hat{O}(x,y,z)=\sum_{j=1}^{J}\sum_{k=1}^{K} b(x_j,y_k,\frac{2R_{j,k}}{v}) \qquad \textbf{(7. 14)}$$

where

$R_{j,k}$ is the distance between the measuring position $(x_j,y_k,0)$ and the point (x,y,z) that is to be migrated,

v the propagation velocity of the medium.

The time $\frac{2.R_{j,k}}{v}$ represents the total travelling time from the transmitting antenna to the point (x, y, z) and back.

For the UWB GPR data, using the antennas off-ground, the two-way travelling time in equation (7.14) has to be modified to take into account the different velocities of the two media (air and ground) and the diffraction on the air-ground interface. This can be done by calculating for each point in the object plane the corresponding migration template in the recorded data. To obtain the point in the migrated image, the summing must be performed along the migration template. This must be repeated for all points in the object plane.

The result of the above described diffraction migration method on a B-scan, recorded with the UWB GPR is shown in Fig. 7-6. The B-scan represents a metal disc with a radius of 5 cm, buried at 6 cm in dry sand. The diffraction hyperbolas on the top of the metal disc are clearly visible in Fig. 7-6 (a). On the migrated image however, the diffraction hyperbolas disappear and the physical dimensions of the targets approach the real dimensions of the target. Note the presence of some artefacts in the migrated image at the left and the right side above the target. These artefacts, typical for the method, are explained by the fact that the summation of the data along a diffraction hyperbole not always tends to zero when no target is present.

The diffraction migration algorithm is easy to implement, but computationally intensive, because the diffraction template on which we have to sum has to be recalculated for each depth. In practice however, the shape of the diffraction hyperbola does not change very much with depth and the same hyperbola can be used for a broad depth range. On the other hand, diffraction migration does not take the physics of wave propagation into account. Therefore more complex algorithms will be introduced.

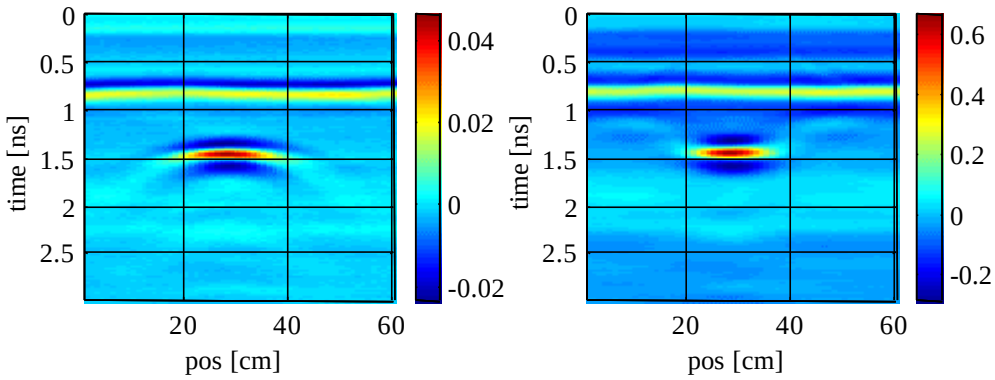

(a) (b)

Fig. 7-6: (a) B-scan of metal disc, buried at 6 cm in dry sand, (b) result after migration, using the diffraction migration algorithm

Kirchhoff-migration

The basic idea in the Kirchhoff-migration is to back-propagate the wavefront, measured in the data-plane (as defined in the exploding source model, see Fig. 7-5), to the object plane at $t = 0$, using an integral solution method to the scalar wave equation. So this migration method involves back-propagation or inverse extrapolation to remove the effects of wave field propagation. In fact the array of receivers recording the data $b(x', y', z' = 0, t')$ in the data plane, denoted here as S', will be replaced by an array of secondary sources, each driven in reverse time by the recorded data. Doing so the migrated image $\hat{O}(x, y, z)$ is calculated as

$$\hat{O}(x, y, z) = \frac{2}{4p\, v} \iint_{S'} \dot{b}(x', y', z' = 0, |\bar{r} - \bar{r}'| / v) \frac{\cos(q)}{|\bar{r} - \bar{r}'|} dS' \qquad \textbf{(7. 15)}$$

where $\dot{b}(x', y', z' = 0, t')$ is the time derivative of the data recorded in the data plane S',

$\bar{r} = (x, y, z)$ the point to be migrated, and

q the angle between the direction $\bar{r}'–\bar{r}$ and the normal to the data plane S'.

The complete development of (7.15) is found in Appendix B.

Comparing the result of the diffraction migration method in (7.14) with the Kirchhoff migration given by (7.15), three differences are observed. First there is the oblique factor $\cos(q)$, that takes into account the fact that the normal to the wave front is not parallel to the normal of the measuring surface. Second there is the spreading factor $\frac{1}{|\bar{r}-\bar{r}'|}$, dealing with the spreading losses of spherical waves. Last, the summation over the diffraction hyperbola has to be taken on the time derivative of the recorded data. So before summation, the time derivative of each A-scan has to be calculated.

Equation (7.15) has to be adapted for the data coming from the UWB GPR with the two antennas off-ground. The same principle as in the diffraction-summation method is used, *i.e*. the summing is performed on a migration template. In (7.15) the travelling time $\frac{|\bar{r}-\bar{r}'|}{v}$ is replaced by the actual travelling time (from transmitting antenna towards the point (x,y,z) to be migrated and back to the receiving antenna). For the calculation of the angle q, the refraction on the air-ground interface has to be taken into account.

For comparison purposes, the Kirchhoff migration algorithm has been applied to the same B-scan as in the previous method. The B-scan in Fig. 7-7 (a), recorded with the UWB GPR, represents a metal disc with a radius of 5 cm, buried at 6 cm in dry sand. The result after migration is shown in Fig. 7-7 (b). The result is obviously better than with the diffraction summation method. The target is more focussed and there are almost no artefacts left on the top of the metal disc.

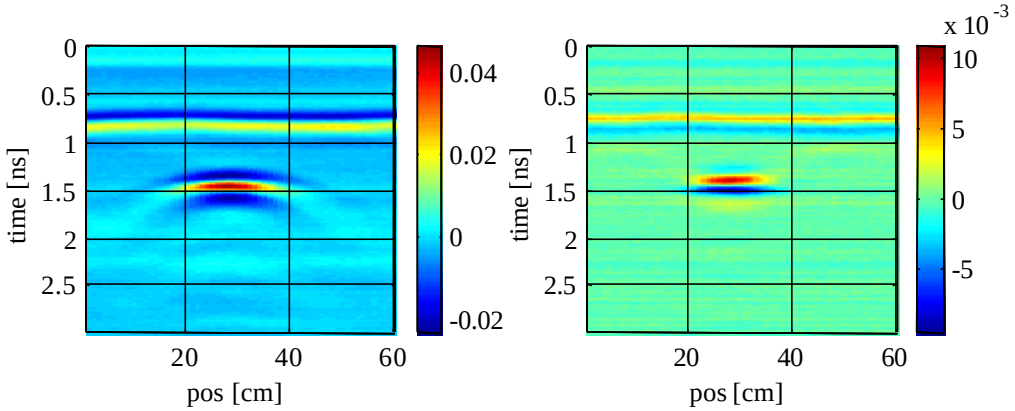

(a) (b)

Fig. 7-7: (a) B-scan of metal disc, buried at 6 cm in dry sand, (b) result after migration, using the Kirchhoff migration algorithm.

Finite-Difference Migration

The finite-difference migration is, just as the Kirchhoff migration, a method that back-propagates the wavefront, measured in the data-plane towards the object plane at $t = 0$. The main difference with the Kirchhoff method is the way of solving the scalar wave equation. The finite-difference migration is based on the differential solution. From the wavefront at time t, it calculates the wavefront at time $t - \Delta t$, using finite-difference approximations, and backpropagates until $t = 0$.

Frequency-Wavenumber Migration

In 1978, Stolt [22] introduced a Fourier transform approach in migrations. Since then, variants on the methods on the original Stolt migration appeared. All these methods are grouped under the name *Frequency-Wavenumber Migration*, or in short f-k migration.

The method is, just like the former two, based on the back-propagation of the scalar wave-equation and can thereby best be explained using the exploding source model. More details about the calculation are found in Appendix B.

If $B(k_x, k_y, 0, w)$ is the Fourier transformation of the data recorded in the data plane, with respect to the x, y and the t co-ordinate, then the migrated image can be calculated as

$$\hat{O}(x, y, z) = \iiint B(k_x, k_y, 0, w) e^{-i(k_x x + k_y y + k_z z)} dk_x dk_y dw \qquad \textbf{(7. 16)}$$

where k_z is a wavenumber defined as

$$k_z = \mathrm{sgn}(w) \sqrt{\frac{w^2}{v^2} - k_x^2 - k_y^2} \qquad \textbf{(7. 17)}$$

Equation (7.16) is the general representation of the f-k migration, also called the *Phase Shift Migration.* The method can deal with variations of velocity as a function of depth. The *Stolt Migration* is a variant on the *Phase Shift Migration,* for a constant propagation velocity. In the special case where $v(z) = v = cst$, equation (7.16) can be further developed by a change of variables from w to k_z. The migrated image becomes

$$\hat{O}(x, y, z) = v^2 \iiint \frac{k_z}{w} B(k_x, k_y, 0, w) e^{-i(k_x x + k_y y + k_z z)} dk_x dk_y dz \qquad \textbf{(7. 18)}$$

The advantage of (7.18) over (7.16) is that (7.18) can be calculated using an inverse Fourier transformation of $B(k_x, k_y, 0, w)$, scaled by $\frac{v^2 k_z}{w}$, *i.e.* the Jacobian of the transformation from w to k_z. This implies a serious reduction of the number of floating point operations for the migration and a gain of calculation time.

Fig. 7-8 (b) shows the result of the Stolt migration on the B-scan representing a metal disc with a radius of 5 cm, buried at 6 cm in dry sand (Fig. 7-8 (a)). In the configuration of the UWB GPR, as the antennas are used off-ground, there is a change in the vertical propagation velocity, and normally the Stolt migration given by (7.18)

can not be used. To solve this problem, a constant mean velocity, somewhere between the propagation velocity in air and in ground, is used for the migration. This is probably the reason why the method performs less good than to the Kirchhoff migration. The artefacts on the left and the right side above the ground are due to the Fourier transformation. They can be avoided by windowing the data, prior to migration.

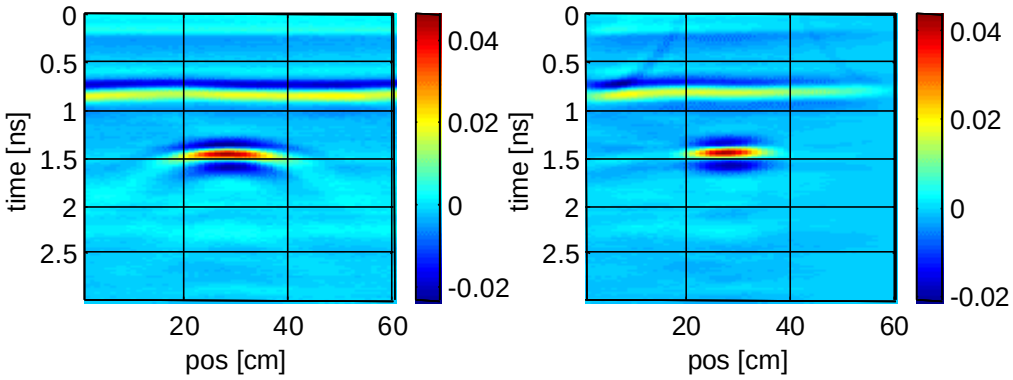

Fig. 7-8: (a) B-scan of metal disc, buried at 6 cm in dry sand, (b) result after migration, using the Stolt migration algorithm

7.4. Migration by deconvolution

In previous section we have concentrated on some existing migration methods. Most of these methods are based on backpropagation of waves. Almost none of these methods however include system aspects of the GPR like the waveform of the excitation source, the impulse response of the antennas, the antenna pattern, etc. Furthermore most of the migration methods consider the ground as being loss-less and without dispersion. It can be expected that an imaging technique that takes into account the characteristics of the system and possibly the characteristics of the ground would perform better. The migration scheme presented in this section is a backpropagation technique based on the deconvolution of the recorded C-scans with the point spread function of the system. This point spread function is a synthetic C-

scan of a fictive point target at a given depth. It includes all the above mentioned system and ground characteristics. The point spread function can be found by forward modelling. By doing so, a very simple and fast migration algorithm, integrating system and ground characteristics, is obtained.

7.4.1. Development of the method

The development of the method is done in the time domain, using the time domain description of the system, presented in Chapter 5. The migration by deconvolution makes only sense if the acquisition process by the GPR is a convolution between the structure present in the subsurface and the point spread function of the system. This can be demonstrated under certain assumptions.

Suppose a co-ordinate system as represented in Fig. 7-9. The antenna configuration is a bistatic configuration and there are only variations in propagation velocity in the downward direction. The 3D data $b(x, y, z = 0, t)$ are recorded on a regular grid by moving the antennas in the xy-plane at z =0.

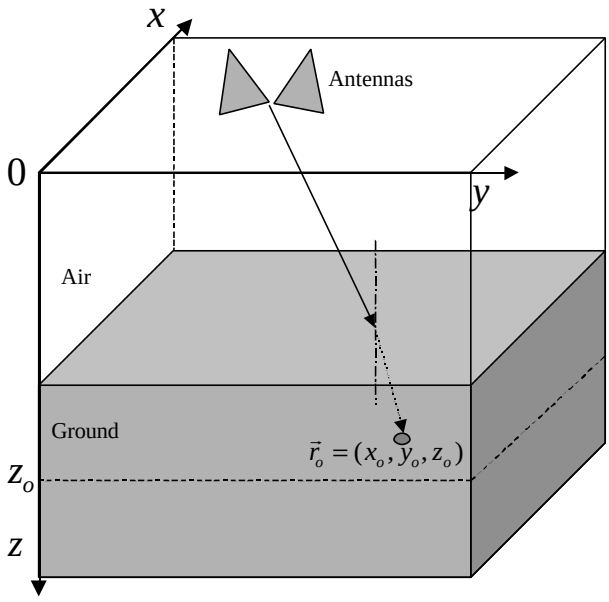

Fig. 7-9: Configuration and representation of the co-ordinate system

Assume in a first time that there is only one small isotropic point scatterer present in the subsurface, located at $\vec{r}_o = (x_o, y_o, z_o)$ and characterised by an impulse response (IR) $\Lambda_o(t_o)$, independent of the incident direction. Note that, in the most general case, the IR of the localised isotropic point scatterer does not necessarily have to be a Dirac impulse as a function of time. For the antennas at any position $\vec{r}_a = (x_a, y_a, z = 0)$, the received voltage, representing an A-scan, can be written according to (5.13) as

$$b(\vec{r}_a, t) = \frac{T_{a-g} T_{g-a}}{8p^2 R_t R_r c} g_d(t) \otimes h_{N,Tx}(\vec{a}_i, t) \otimes \Lambda_o(t) \otimes h_{N,Rx}(-\vec{a}_s, t) \otimes \frac{dVs(t - t_d)}{dt} \qquad \textbf{(7. 19)}$$

where t_d represents the exact two-way travelling time between the antennas and the point target, taking into account the different propagation velocities in the media.

By grouping all the factors, except for the IR of the point target, in one factor $w(\vec{r}_a, \vec{r}_o, t)$, equation (7.19) becomes

$$b(\vec{r}_a, t) = w(\vec{r}_a, \vec{r}_o, t) \otimes_t \Lambda_o(t) \qquad \textbf{(7. 20)}$$

The symbol $\otimes_t$ is introduced to clearly indicate that the convolution in (7.20) is a convolution in time: $b(\vec{r}_a, t) = \int_t w(\vec{r}_a, \vec{r}_o, t - t)\Lambda_o(t)dt$. For a given configuration, all the factors in (7.19) are known, hence $w(\vec{r}_a, \vec{r}_o, t)$ can be easily calculated. Furthermore, for the antennas at $z = 0$ and the point scatterer at a fixed depth $z = z_o$, the response $w(\vec{r}_a, \vec{r}_o, t)$ is a function of $\vec{r}_o$ and $\vec{r}_a$ only by their difference, and (7.20) can be written as

$$b(\vec{r}_a, t) = w(\vec{r}_a - \vec{r}_o, t) \otimes_t \Lambda(r_0, t) \qquad \textbf{(7. 21)}$$

If an object can be modelled by a set of independent small isotropic point scatterers, all at approximately the same depth $z = z_o$, the output voltage $b(\vec{r}_a, t)$ will be a

combination of the contribution of each individual point scatterer, that is clearly a convolution in space if we assume that the operation is linear:

$$b(x_a, y_a, t) = \iint_{x,y} \int_t w(x_a - x, y_a - y, z_o, t - t')\Lambda_{zo}(x, y, t')dt'\,dxdy \qquad \textbf{(7. 22)}$$

Equation (7.22) represents a space-time convolution along the co-ordinates x, y and t, and can be written as

$$b(x, y, t) = w(x, y, z_o, t) \otimes_{x,y,t} \Lambda_{zo}(x, y, t) \qquad \textbf{(7. 23)}$$

where $\Lambda_{zo}(x, y, t)$ is a 3D matrix, called the scattering matrix [19], and contains the responses associated with the distributed point scatterers at approximately a depth z_o. The symbol $\otimes_{x,y,t}$ denotes a space-time convolution along the co-ordinates x, y and t. The 3D matrix $w(x, y, z_o, t)$ represents the point spread function of the UWB GPR system for a depth z_o and is found by replacing the scattering matrix in (7.23) by a Dirac impulse in space and time:

$$\Lambda_{zo}(x, y, t) \equiv d(x, y, z - z_o)d(t) \qquad \textbf{(7. 24)}$$

In practice the 3D point spread function $w(x, y, z_o, t)$ is calculated by using (7.19) for different antenna positions $\vec{r}_a$ on a regular grid in the xy-plane at $z = 0$ and a small fictive point scatterer with IR $d(t - t_d)$, at a depth z_o. In other words it can be seen as a synthetic C-scan of a small fictive point scatterer. Fig. 7-10 shows the 3D point spread function of the system at a depth of 6 cm below the air-ground interface (with the antennas 25 cm above the ground). In the point spread function, as it is obtained by forward modelling, all the information on the system like the waveform of the source, the IR of the antennas, the antenna pattern, the attenuation and dispersion in the ground, etc. are included. Note that for the implementation of (7.23), the apex of the hyperboloid in Fig. 7-10 has to be centred in the origin of the 3D image, *i.e.* the

top corner of the 3D volume. If not, the convolution with the point spread function will introduce a displacement of the objects in the scattering matrix.

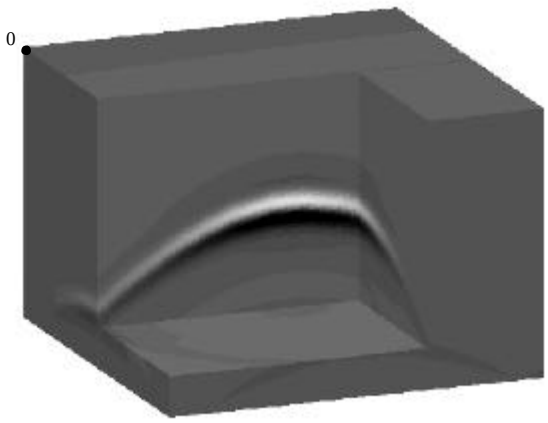

Fig. 7-10: Synthetic C-scan of a fictive point scatterer at a depth of 6 cm below the air-ground interface

Although the point spread function $w(x, y, z_o, t)$ is space variant (function of z_o), its shape will not change very much with depth. In practice, the point spread function for a given depth can be used for a broad depth range. As a consequence, the space-time convolution (7.23) can by considered as space (depth) invariant and the image of the 3D scattering matrix $\hat{\Lambda}(x, y, t)$ can be calculated in one step by

$$\hat{\Lambda}(x, y, t) = b(x, y, t) \otimes^{-1}_{x,y,t} w(x, y, z_o, t) \qquad \textbf{(7. 25)}$$

where $\hat{\Lambda}(x, y, t)$ denotes the spatial image of $\Lambda_{zo}(x, y, t)$, *i.e.* the migrated image,

$b(x, y, t)$ is the recorded C-scan that is to be migrated,

$w(x, y, z_o, t)$ the point spread function for a fixed depth $z = z_o$, and

$\otimes^{-1}_{x,y,t}$ a deconvolution in x , y and t .

7.4.2. Implementation of the migration method

From the mathematical point of view, solving equation (7.25) can cause some problems. Because of the band-limited nature of the system and the effects of noise, equation (7.25) is a classical ill-posed problem. A fast and computational not intensive mathematical solution for the deconvolution is to perform it in the frequency-wavenumber domain, by means of a Wiener filter [23]. A Wiener filter is an optimal filter that minimises the variance of the error between the restored image and the original image before degradation, under the assumption of a signal-independent noise, a linear degradation and stationarity of the images.

Let $B(k_x, k_y, w)$ be the 3D Fourier transform of the data recorded $b(x, y, t)$, with respect to the x, y and the t co-ordinates:

$$B(k_x, k_y, w) = \iiint b(x, y, t) e^{ik_x x + ik_y y - iwt} dx dy dw \qquad \textbf{(7. 26)}$$

Taking the Wiener filter approach, the restored image in the frequency-wavenumber domain is given by

$$\hat{\Lambda}(k_x, k_y, w) = \frac{B(k_x, k_y, w) W^*(k_x, k_y, w)}{W(k_x, k_y, w) W^*(k_x, k_y, w) + \dfrac{P_n(k_x, k_y, w)}{P_\Lambda(k_x, k_y, w)}} \qquad \textbf{(7. 27)}$$

where $W(k_x, k_y, w)$ is the 3D Fourier transformation of the calculated point spread function,

$W^*(k_x, k_y, w)$ its complex conjugate,

$P_n(k_x, k_y, w)$ the spectral density of the noise in the image , and

$P_n(k_x, k_y, w)$ the spectral density of the original image.

The main problem with the Wiener filter is that it can be difficult to get a good estimation of the spectral density of the noise and the spectral density of the image before degradation, which is *a priori* not known. A classical solution is to replace the ratio of the two power spectral densities by a constant parameter m, also called water level parameter. It will prevent (7.27) of becoming too large for very small values of $W(k_x, k_y, w)$.

Finally the migrated image is given by the inverse 3D Fourier Transform of $\hat{\Lambda}_{zo}(k_x, k_y, w)$:

$$\hat{\Lambda}(x, y, t) = \frac{1}{2p} \iiint \hat{\Lambda}(k_x, k_y, w) e^{-i(k_x x + k_y y - wt)} dk_x dk_y dw \qquad \textbf{(7. 28)}$$

The migration scheme is resumed in the following steps:

1. The point spread function is calculated for a given soil type and depth. The depth is chosen to be the most likely depth for an object. In our application a burial depth of 6 cm is always chosen. The calculation of the point spread function only has to be done once.
2. The 3D Fourier transform of the recorded data is calculated by (7.26).
3. The data is filtered by the Wiener filter as in (7.27).
4. The inverse 3D Fourier Transform of the filtered data is calculated, represented in (7.28), resulting in the migrated image.

As already mentioned, this migration scheme is very simple and not computational intensive. Suppose a C-scan of 32*32*256 points representing an area of 64 cm by 64 cm with a step of 2 cm in both lateral directions. The 3D Fourier transformation, the filtering and the inverse transformation of this C-scan (steps 2-4 of the migration scheme) only takes 76 Mflops, which means that it can easily be implemented in real time. The migration of a C-scan of 64*64*256 points takes approximately 246 Mflops.

7.4.3. Discussion

Influence of the spatial invariance approximation of the point spread function

The key-point of the whole migration method lies in the approximation of considering the point spread function as space invariant. It permits to calculate $\hat{\Lambda}(x,y,t)$ by (7.25) in one step. This approximation is based on the assumption that the shape of the point spread function does not change very much with depth. Suppose there is only one object in the ground, at approximately a depth of 10 cm. Ideally, the deconvolution of the raw C-scan should be done with a point-spread function, calculated for objects at 10 cm of depth. As *a priori* we do not know the depth of the buried object, the raw C-scan will be deconvolved with a point spread function calculated for the most probable depth of an object, *i.e.* 6 cm. To have an idea of the influence of this error on the migration results, the following verification was done. The point spread function is calculated for a depth of 6 cm. This point spread function is then used to migrate synthetic images of point targets respectively at 2 cm, 6 cm, 10 cm and 15 cm of depth in the ground. For all of the three cases, the same water level parameter m is used in the Wiener filter to perform the deconvolution. The results after migration are shown in Fig. 7-11. The migrated image of the point target at 6 cm (Fig. 7-11 (b)) gives the best focussed image, which is logical because the point spread function, used for the deconvolution, was calculated for targets at 6 cm of depth. The results after migration of the other three point targets at 2 cm, 10 cm and 15 cm of depth give less focussed but still acceptable results.

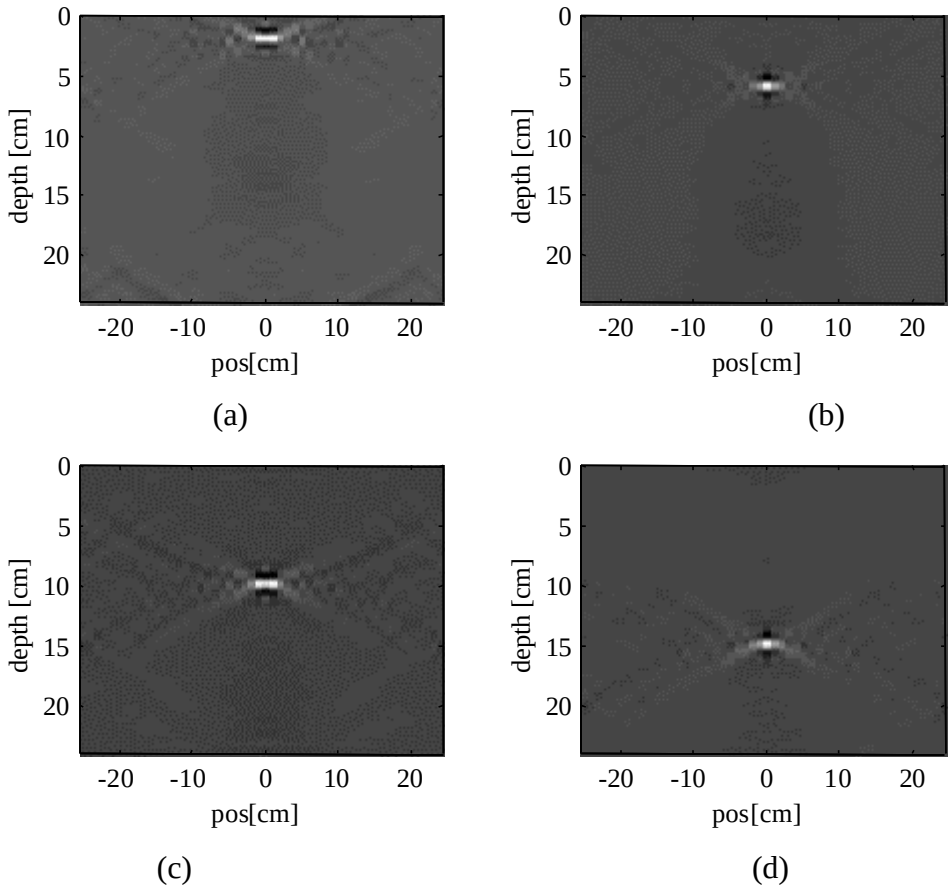

Fig. 7-11: The influence of the space invariant approximation of the point spread function

(a) migrated image of the point targets at 2 cm
(b) migrated image of the point targets at 6 cm
(c) migrated image of the point targets at 10 cm
(d) migrated image of the point targets at 15 cm

For comparison, the result of the Kirchhoff migration method on the synthetic image of the point targets at 6 cm is given in Fig. 7-12. It is clear that the result after the Kirchhoff migration is less focussed than any of the results in Fig. 7-11, which brings us to the conclusion that the approximation of considering the point spread function as space invariant is acceptable.

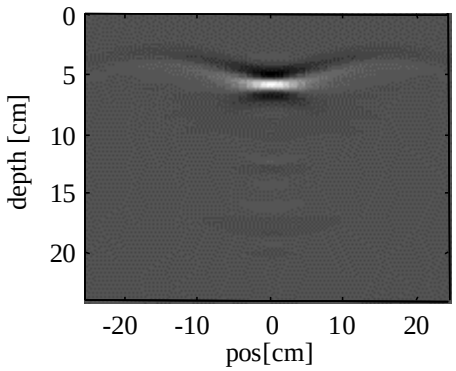

Fig. 7-12: Migrated image of the point targets at 6 cm after Kirchhoff migration

Note that for the migration of the synthetic images, the Kirchhoff migration method is put in an unfair position compared to the migration by deconvolution. The synthetic images are obtained by forward modelling, using the same model as for the calculation of the point spread function. Applying the migration methods on real images however, we also noticed that the migration by deconvolution gave systematically better focussed images than the Kirchhoff migration. Fig. 7-13 shows a B-scan of a PMN mine at 5 cm of depth, after migration by deconvolution (Fig. 7-13 (a)) and after Kirchhoff migration (Fig. 7-13 (b)). It can be seen that the image on the left is slightly more focussed. Furthermore on images with a lot of clutter or a very weak reflection of the object, the object is in general more visible when the image is restored by the migrated by deconvolution method than by the Kirchhoff migration method.

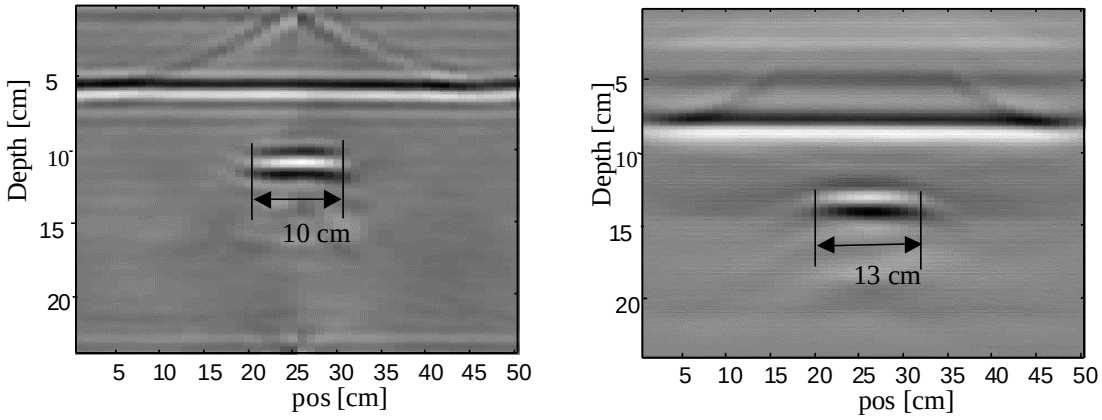

(a) (b)

Fig. 7-13: PMN at 5 cm of depth, (a) after migration by deconvolution, and (b) after Kirchhoff migration

Spatial resolution in x- and y- direction

In general, the spatial resolution of a GPR system depends on a lot of system and ground parameters, *e.g*. the dimensions of the combined antenna footprint, the bandwidth of the system, the migration method that is used, the losses in the ground, etc. The migrated image in Fig. 7-11 (b) gives an idea of the spatial resolution one could expect from the laboratory UWB GPR after migration by deconvolution. The spatial resolution in the x-direction of the single point target in Fig. 7-11 (b) is 2 cm (the spatial resolution is measured as the 3dB width of the grey-values of the target in the migrated image). Two point scatterers with equal strength can be easily distinguished from each other if they are separated by 4 cm, as shown in Fig. 7-14. Note that these resolution figures must be considered as best cases. First of all, the deconvolution is done with the point spread function calculated for the exact depth. Secondly the results are obtained on synthetic images generated by the same system model and with very little noise present in the images, hence the deconvolution with the Wiener filter will be very successful, leading to a high resolution. If more noise is present in the images, the resolution of the migrated image will decrease due to a decreasing bandwidth of the Wiener filter. Further, the resolution will also decrease if the ground becomes more lossy. Higher losses will reduce the width of the hyperbole, which is equivalent to a reduction of the length of the synthetic antenna.

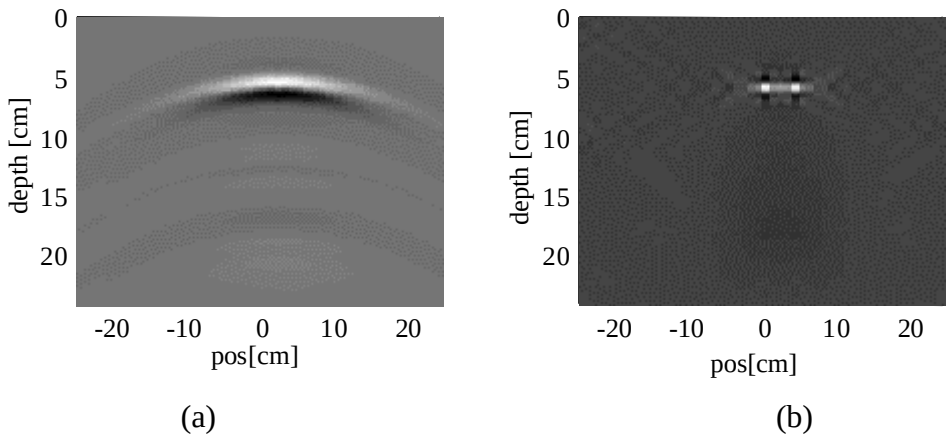

Fig. 7-14: (a) Synthetic B-scan of two point targets at 6 cm of depth, separated by 4 cm, (b) same B-scan after migration by deconvolution

Analogy with imaging techniques

It is shown in Section 7.4.1 that under certain assumptions the acquisition process by the GPR is a convolution between the structure present in the subsurface and the point spread function of the system. Similar conclusions are found in the electromagnetic imaging theory, using the same assumptions, but a different target modelling. Electromagnetic imaging is a linearised inversion scheme that approximates the field inside the scatterer by the incoming field and thereby can be seen as a subclass of the inverse scattering problems. In electromagnetic imaging, three domains are defined: the source and receiver domain where respectively the sources and receivers are located and the scattering domain, where the objects are located. The objects are modelled by an object function, also called a contrast function $c(\vec{r})$, which is related to the constitutive parameters of the object. In general, the scattered field in the frequency domain $E_{sct}(\vec{r},w)$ at a point $\vec{r}$ belonging to the receiver domain is described by an integral representation

$$E_{sct}(\vec{r},w) = -\int_{\vec{r}'\in D_{sct}} g(\vec{r},\vec{r}',w)c(\vec{r}')E(\vec{r}',w)d\vec{r}' \qquad \textbf{(7. 29)}$$

where $g(\vec{r},\vec{r}',w)$ is the Green function and D_{sct} the scattering domain. Note that for simplicity, the scalar version is described. $c(\vec{r})$ serves as an unknown in the inverse scattering problem. A way to linearise the inversion problem is to introduce the Born approximation [21]. For weak scatterers, *i.e.* scatterers with a low contrast, the total field in the volume integral in (7.29) can be approximated by the incoming field,

$$E(\vec{r}',w) \approx E_{inc}(\vec{r}',w) \qquad \textbf{(7. 30)}$$

Hence (7.29) becomes

$$E_{sct}(\vec{r},w) = -\int_{\vec{r}'\in D_{sct}} g(\vec{r},\vec{r}',w)\, c(\vec{r}')E_{inc}(\vec{r}',w)d\vec{r}' \qquad \textbf{(7. 31)}$$

It is shown in [24] that by considering a monostatic GPR configuration and describing the finite length antennas with an effective point source approximation, equation (7.31) can by rewritten as

$$E_{sct}(\vec{r},w) = -\int_{\vec{r}'\in D_{sct}} W(\vec{r},\vec{r}',w)\, c(\vec{r}')\, S(w)\, d\vec{r}' \qquad \textbf{(7. 32)}$$

where $W(\vec{r},\vec{r}',w)$ is called the two-way wave field extrapolator, describing the propagation of the scalar field from the source to the location $\vec{r}'$ in the scattering domain, and back to the receiver. $S(w)$ contains the frequency information of the source. For antennas at a fixed height above the ground and the object at a given depth $z = z_o = cst$, and no lateral variation of the propagation velocity in the subsurface, the two-way wave field extrapolator is only function of the difference $\vec{r} - \vec{r}'$ and (7.33) can be written as

$$E_{sct}(x_a, y_a, w) = -\int_{D_{sct}} W(x_a - x_o, y_a - y_o, z_o, w)\, S(w)\, c(x_o, y_o)\, dV \qquad \textbf{(7. 33)}$$

where $(x_a, y_a, z_a = cst)$ are the co-ordinates of the antennas, and

$(x_o, y_o, z_o = cst)$ are the co-ordinates of the object.

This means that in the space-frequency domain the scattered field can be presented as a spatial convolution between the contrast function at a depth z_o and the two-way wave field extrapolator for that depth z_o. Note that for this result the same assumptions had to be made as in Section 7.4.1, *i.e.* objects at a fixed depth and no lateral variations in the propagation velocity.

Consideration on the modelling of the target

In the electromagnetic imaging approach the target is modelled by a contrast function and the Born approximation is applied. This means that the scattering sources are

considered to be independent of each other. In the approach we took in Section 7.4.1, the object is modelled by a set of independent point scatterers, each characterised by an IR $\Lambda_o(\vec{r}_o, t_o)$ that can be different from a Dirac function in time. In both cases it is shown that the acquisition process by a GPR is a convolution, but due to the difference in modelling the object, the interpretation of the results after migration are different. The difference however between the two models and the interpretation of the results is subtle. The space that we want to image has in reality four dimensions: x, y, z to indicate the position of targets, and the time dimension t, containing information on the two-way travelling time to the targets and on their impulse responses. If raw C-scan data are recorded the number of dimensions is reduced from four to three by considering the time axis parallel to the z-axis. Doing so we make a mistake that leads to an unfocussed image. To avoid this defocusing, migration methods are applied in order to physically bring the time axis parallel to the z-axis. If we now represent the migrated C-scan in a three dimensional space, the image will be focussed, but we will still be unable to separate the z co-ordinate from the time variable. In the electromagnetic imaging this ambiguity is solved by taking an object function $c(\vec{r}')$ that is only function of the spatial co-ordinates and not function of w. As a consequence, each reflection in the migrated image at a given depth has to be produced by a change in contrast at that depth. This model will work good if the Born approximation holds. In the application of AP mines, the Born approximation does not always hold. In actual applications, a permittivity contrast of over a 100% is easily obtained and the boundaries of an object will be overestimated. In the development of the migration method in Section 7.4.1 we anticipated on this by modelling the object as a set of small point scatterers, each with an IR $\Lambda_{zo}(t)$ different from a Dirac function. In this approach the ambiguity between time and depth is deliberately not solved. Each reflection in the migrated image is a scattering centre produced by a point scatterer at that location or above that location, because each isotropic point scatterer can have an IR different from a Dirac function. As already said, the difference lies in the interpretation of the migrated image. In our approach we recognise that the depth information on an object does not correspond with the physical dimensions of the object. To illustrate the above, let us go back to Fig. 5-2 in Chapter 5, representing the backscattered time domain signal on a dielectric cylinder in free space. In the signal, certain scattering centres appeared later in time than the

reflection on the back of the target. In the Born approximation, this would mean that there are reflections coming from behind the object, where there is no dielectric contrast present. This is physically impossible. The explanation is simple. The scattering centres, which appear later in time, are the products of other scattering mechanisms like creeping waves etc., which in the Born approximation are not allowed. In the modelling we applied in our migration method, we can deal with these other scattering mechanism by considering impulse responses that can be different from a Dirac impulse. The only scattering centre of which we are sure that it will be correctly positioned in each A-scan is the scattering centre corresponding with the specular reflection on the object, indicating the top contour of the object.

7.4.4. Results of the migration method

Considering the poor results of the UWB signal processing techniques on A-scans, we decided to concentrate our work on the interpretation of C-scans in the hope to retrieve information on the shape and dimensions of the buried target. In the previous section we concluded that the depth information is ambiguous, hence the most reliable information on the shape and dimensions of the object will be found in the x- and the y-directions. Therefore we will systematically show projections of the whole (or a part of the) C-scans on a horizontal plane. The projections are the results of the summation of the energy per A-scan:

$$c(x,y) = \sum_{i=n_1}^{n_2} b(x,y,i)^2 \qquad \text{with} \qquad 1 \le n_1 < n_2 \le N \tag{7. 34}$$

Results of indoor trials

The migration by deconvolution is applied on data taken by the laboratory UWB GPR, with the antennas mounted on the indoor xy-scanning table, as described in Chapter 6. The data are acquired over an area of 50 cm by 50 cm with a step of 1 cm in both x- and y-direction. Fig. 7-15, Fig. 7-16 and Fig. 7-17 show respectively the results of the migration method on a PMN mine, a brick of dimensions 15*9*6 cm and a piece of 20 cm barbed wire, all buried at 5 cm of depth in sand. The 3D representations of the raw data (subplots (b)) and the migrated data (subplot (c)), are obtained by performing a Hilbert transform on each individual A-scan to find its envelope. The data are then plotted by the iso-surface 3D plot function of MatLab, highlighting all the pixels of a given intensity. The vertical axis is a time axis in 10^{ths} of ps. In the lower right corner of each image, the two-dimensional C-scan representation, given by (7.34), of the migrated image is shown. For clarity, the ground reflection is omitted in Fig. 7-16 and Fig. 7-17. Looking on the objects from above, the round shape of the PMN mine becomes very clear, whereas the shape of the brick is more rectangular. This means that the (oval) footprint of the antennas has successfully been deconvolved from the recorded data. The shape of the barbed wire in Fig. 7-17 (d) can be easily distinguished from the other two shapes and even contains the three sets of pins, present on the real wire. Note that the dimensions of the objects in the migrated images approach the x- and y-dimensions of the real objects. These three examples show that it is possible to extract the shape and dimensions of a buried object out of the migrated data collected by the UWB GPR. The same three data sets were also migrated by the Kirchhoff migration method. The migrated images were less focussed and the oval shape of the antenna footprint was still visible in the migrated image.

(a)

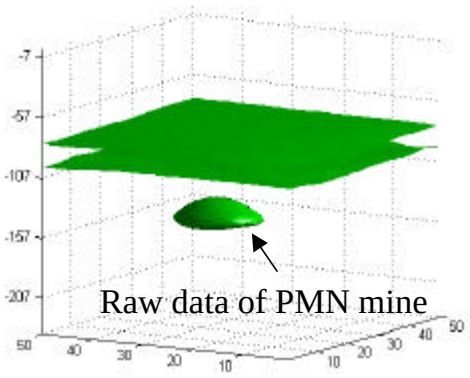

(b)

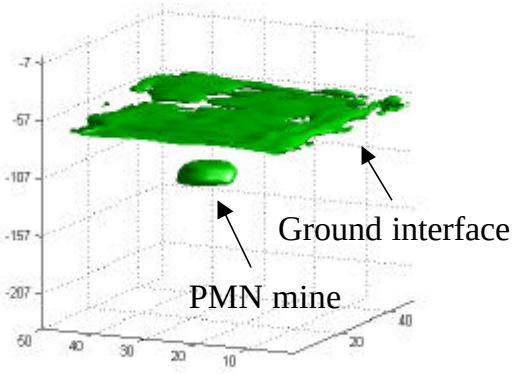

(c)

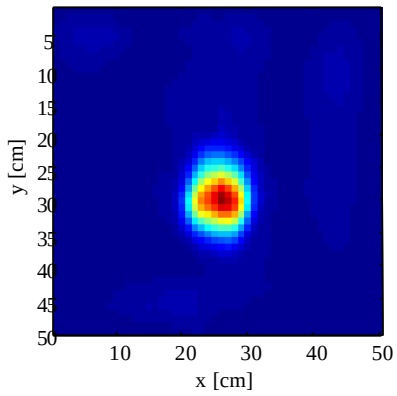

(d)

Fig. 7-15: Migration by deconvolution applied on a PMN mine (diameter of 11 cm) buried at 5 cm

(a) Photo of PMN mine
(b) 3D C-scan representation of raw data
(c) 3D C-scan representation of migrated data
(d) 2D C-scan representation of migrated data

(a)

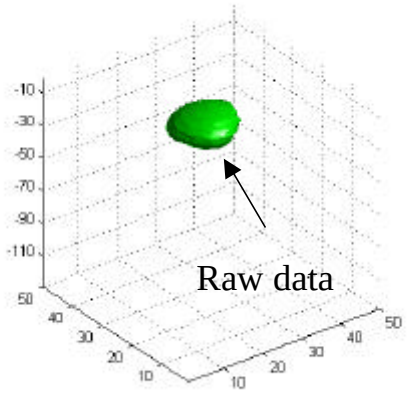

(b)

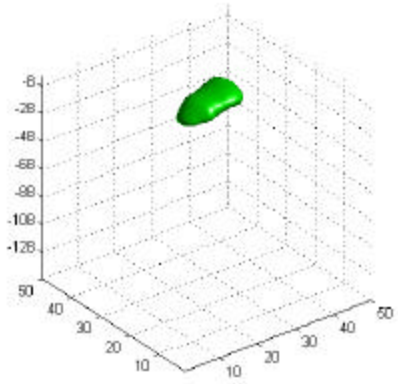

(c)

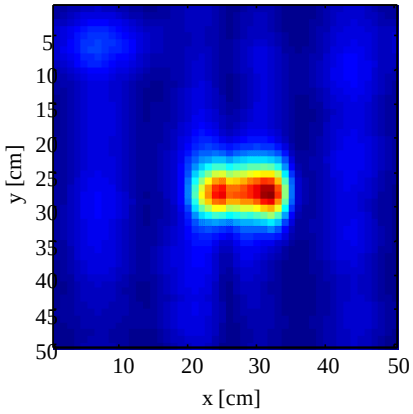

(d)

Fig. 7-16: Migration by deconvolution applied on a brick (15*9*6cm) buried at 5 cm

(a) Photo of the brick

(b) 3D C-scan representation of raw data

(c) 3D C-scan representation of migrated data

(d) 2D C-scan representation of migrated data

(a)

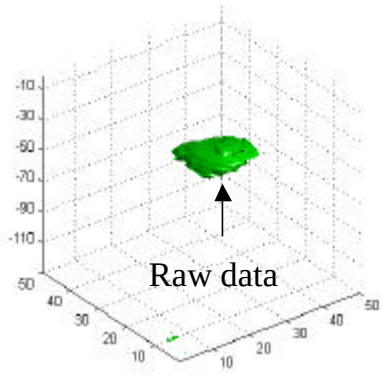

(b)

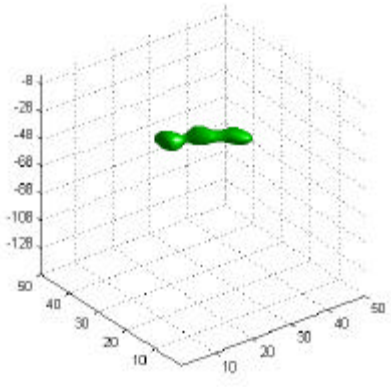

(c)

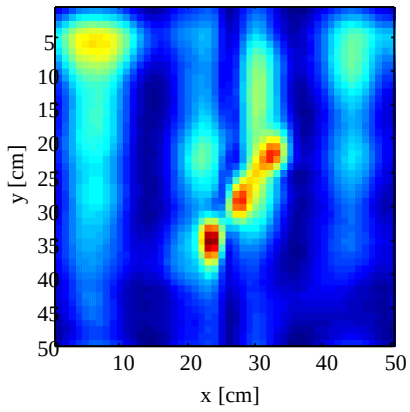

(d)

Fig. 7-17: Migration by deconvolution applied on barbed wire (length of 20cm) buried at 5 cm

(a) Photo of the barbed wire

(b) 3D C-scan representation of raw data

(c) 3D C-scan representation of migrated data

(d) 2D C-scan representation of migrated data

The aim of migration is to focus reflections on objects back into the true physical shape of the object but also into its true position. To illustrate the latter, we show in Fig. 7-18 (a) the raw date on an oblique mine. The mine was buried under an angle of about 30° in dry sand, with the highest point of the mine at a depth of 5 cm. In the raw B-scan at the left, the strongest reflections on the mine are found in the lower right corner of the image, whereas in reality the mine is situated in the middle of the image, indicated by the rectangular box in the image. The explanation for this shift is simple. When the antennas are right above the oblique mine, the mine will have a strong reflection in a direction away from the receiving antenna. For the antennas in the direction perpendicular to the flat top of the mine, the reflections on the mine towards the receiving antenna will be stronger than in the case the antennas are right above the oblique mine, leading to a displacement of the target in the raw data. After migration by deconvolution however, the target is found in its true position, as shown in Fig. 7-18 (b). The migrated image not only shows the object in its true position, but also clearly shows that the object is oblique. Indeed, due to the different backscatter mechanism in the object, the dimensions of the object in the z-direction can be overestimated, but the position (in time or space) of the first reflection on the object (the specular reflection) will be correct and reliable. Hence the reconstruction of the top contour of buried objects will be correct. Other migration methods, like Kirchhoff migration and Stolt migration were also applied on the same data, but with less good results than the migration by deconvolution method. Fig. 7-18 (c) shows the result after Kirchhoff migration. The migrated image is better than the raw one, but the Kirchhoff migration is not able to bring the target completely back in its actual position.

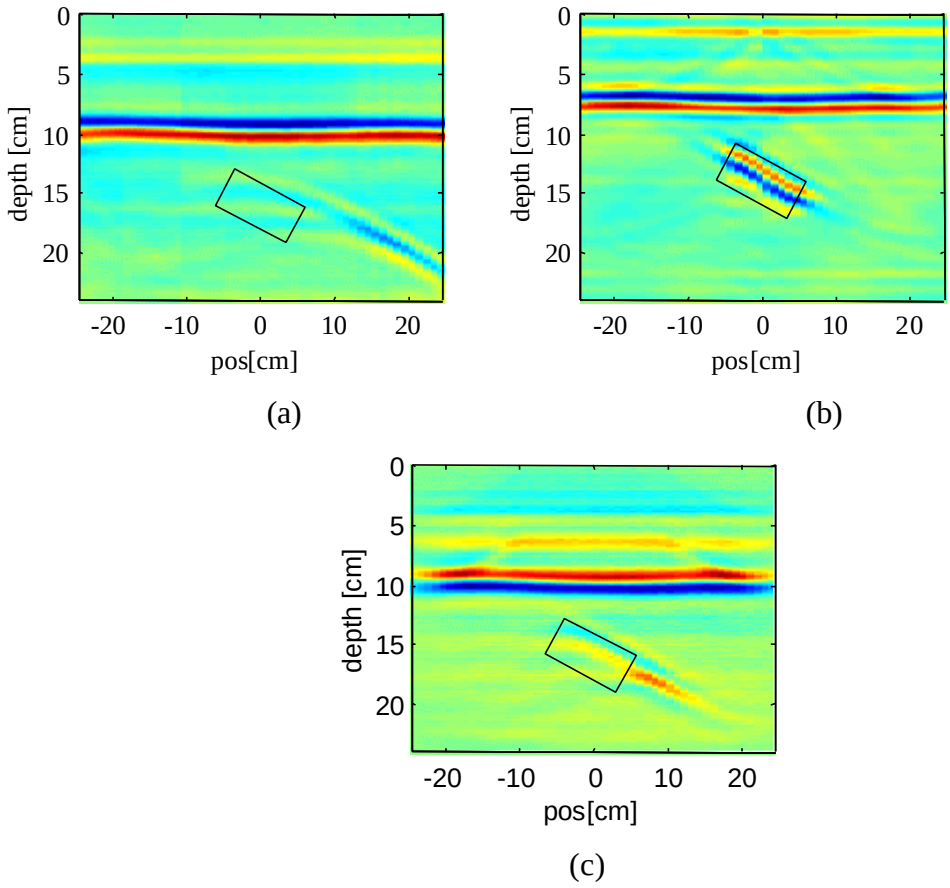

Fig. 7-18: Oblique PMN mine under an angle of 30°

(a) Raw data

(b) After migration by deconvolution

(c) After Kirchhoff migration

Results of outdoor trials

The previous results are obtained on data that is acquired in the laboratory, where all conditions are well controlled and where the air-ground interface is flat. In reality this is not the case. Ground characteristics like permittivity and attenuation are often not known and have to be estimated. The air-ground interface can be very rough and can introduce additional clutter, which eventually might interfere with the reflections on the target, like presented on Fig. 7-19. Furthermore, the ground is not always homogeneous and it can be expected that the UWB GPR, which yields a high resolution, is sensible to these inhomogeneities.

In this subsection some results of outdoor trials are presented. The trials were held on the test site in Meerdaal, in August 2000. At that moment, the objects were already more than three years in place. After a lot of rain during the summer, the soil was quite wet and it seemed that the attenuation of the soil was too high to get good results on the smallest AP mines. We already discussed this problem, which is partially due to the laboratory UWB GPR. The larger AP mines and mine-like targets gave good results.

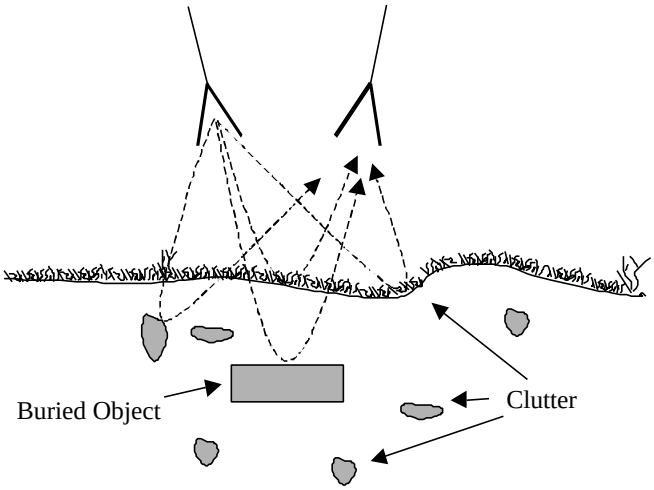

Fig. 7-19: Clutter introduced by the rough air-ground interface and inhomogeneities in the ground

The data represented in the next three figures is acquired over an area of 50 cm by 50 cm in steps of 2 cm (which is still small enough to avoid aliasing in the x- and y-direction).

Fig. 7-20 shows a 2D representation of a B-scan and a C-scan of a PMN mine, buried in gravel at a depth of 5 cm, before and after migration. In the images of the raw data there is a lot of clutter present and the shape of the mine is not clear. After migration, most of the clutter disappeared and the circular shape and dimensions of the mine becomes correct.

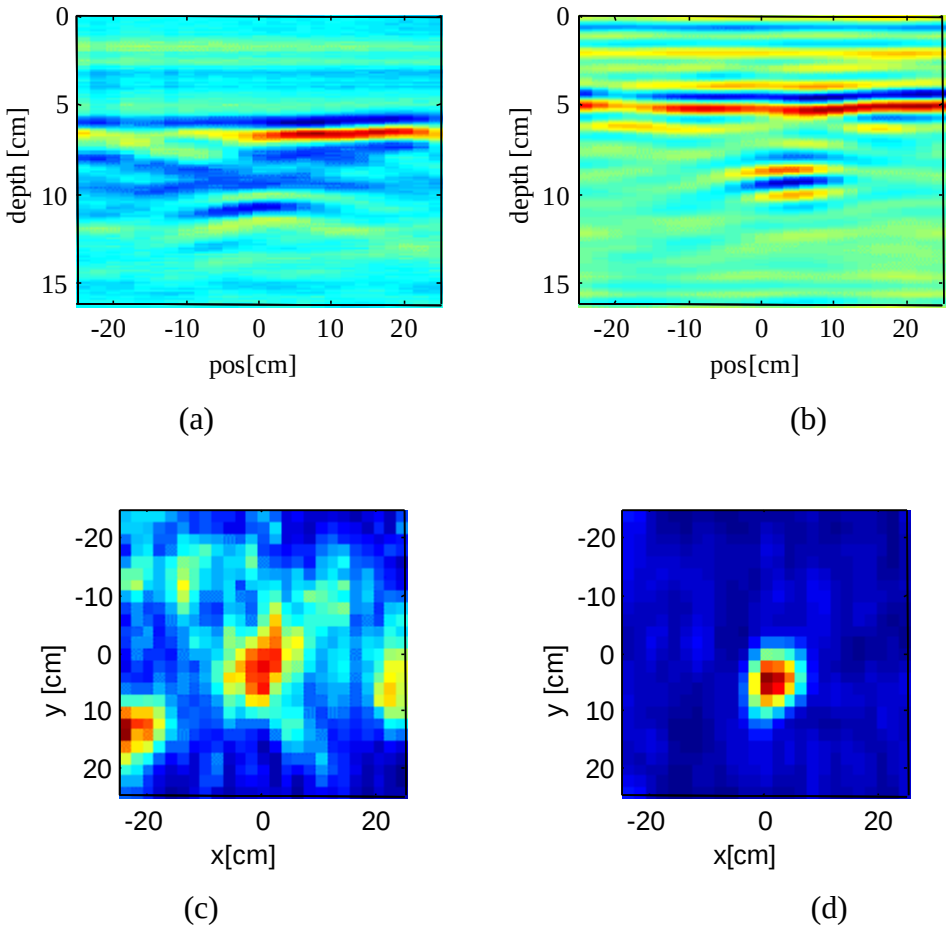

Fig. 7-20: PMN mine in gravel at 5 cm of depth

(a) B-scan of raw data

(b) B-scan of migrated data

(c) 2D C-scan representation of raw data

(d) 2D C-scan representation of migrated data

Fig. 7-21 shows a PMN mine that was laid on the surface of the ground. On the migrated B-scan, the mine is clearly distinguishable from the air-ground interface. The migrated B-scan even shows that the mine is a little oblique. Just like in previous figure, the shape of the target becomes more clear in the 2D C-scan representation after migration.

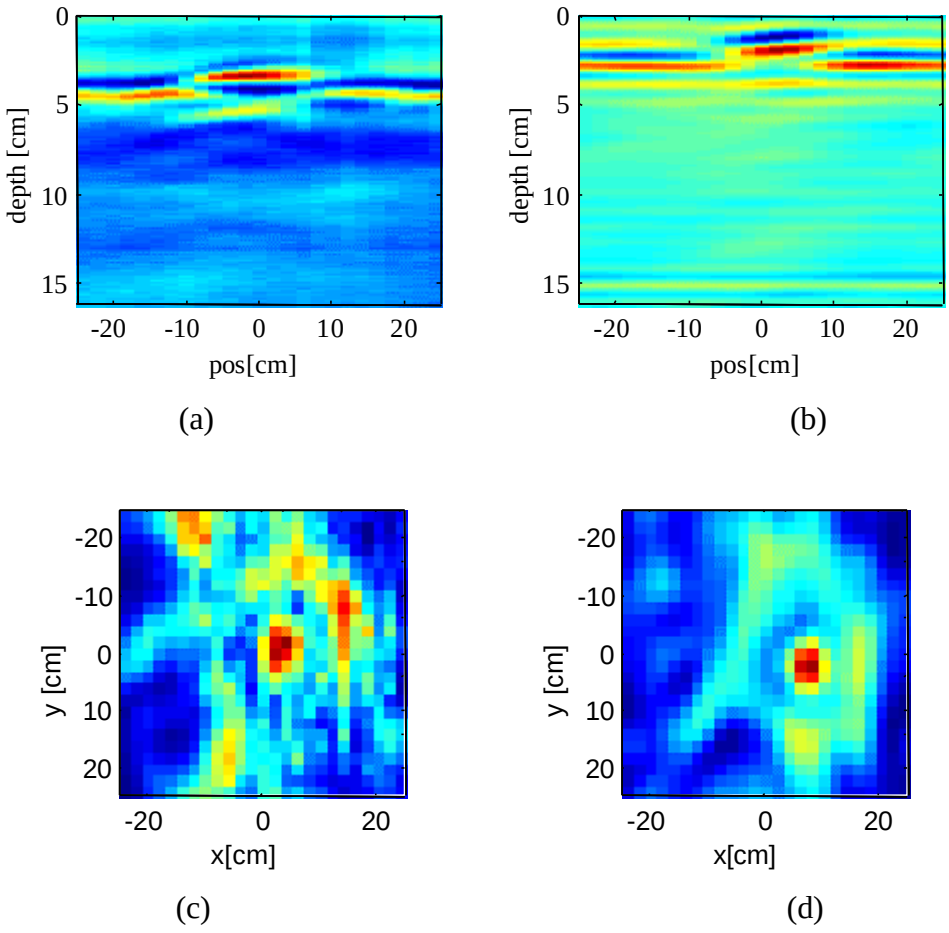

Fig. 7-21 : PMN mine laid on the surface

(a) B-scan of raw data

(b) B-scan of migrated data

(c) 2D C-scan representation of raw data

(d) 2D C-scan representation of migrated data

Fig. 7-22 shows the result on an (empty) wine bottle buried in sand at a depth of about 7 cm. During the years the bottle is probably partially filled with sand, which explains the low contrast in the images, even after migration.. The result after migration however is interesting. The 2D C-scan representation of the migrated data reveals that the shape of the object is not round and that the object is oriented from the left to the right in the image and not vertically like one could expect from the 2D C-scan representation of the raw data.

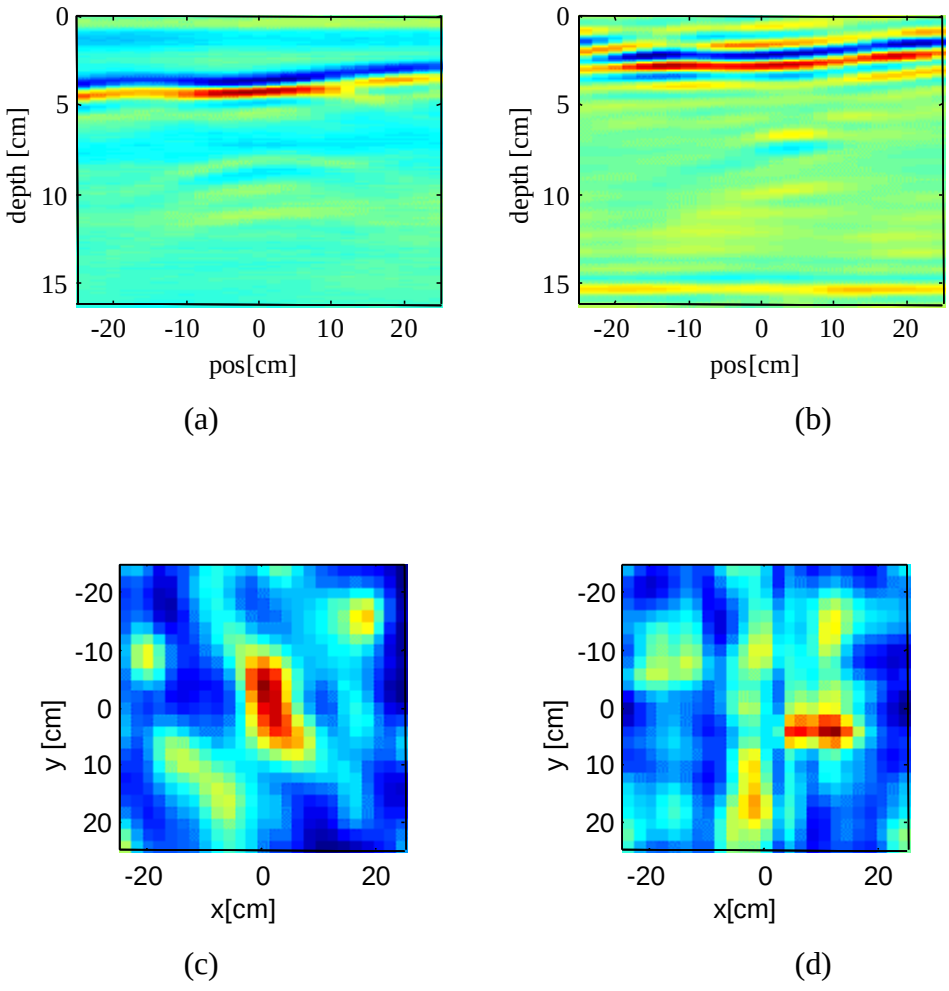

Fig. 7-22 : Bottle in sand at a depth of 7 cm

(a) B-scan of raw data

(b) B-scan of migrated data

(c) 2D C-scan representation of raw data

(d) 2D C-scan representation of migrated data

7.5. Summary

Because anti personnel landmines are small objects and often shallowly laid, a large bandwidth is needed for a better depth resolution and a more detailed echo. In a first part of the chapter we presented some UWB signal processing techniques on A-scans, based on Prony-type methods and on time-frequency analysis. Despite the larger bandwidth of the system, UWB signal processing techniques on the A-scans seem to have limited success. This is probably due to the low Q factor of the targets. None of these methods seems to be robust enough to be used for classification purposes. The conclusions drawn out of the study on the UWB signal processing techniques on A-scans are considered as preliminary. However they did not convince us to invest more in this direction.

We therefore oriented our work towards the exploitation of the C-scans, to investigate the possibility of retrieving information on the shape and dimensions of the targets. The raw C-scans recorded by a GPR are often difficult to interpret for an operator. Due to the beam-width of the antennas, a target in the ground is already seen by the GPR system even when it is not exactly under the antennas. As a consequence, the recorded data will be unfocussed. Focussing techniques to reduce the influence of the beamwidth of the antennas are called migration techniques. Most of the existing migration techniques however do not take into account the characteristics of the acquisition system and the ground characteristics. We therefore proposed a migration technique, called the migration by deconvolution. The novelty of the algorithm is that it uses the time domain model of the GPR and hence does take into account the system and ground characteristics. The migration method is simple and fast. We calculate by forward modelling a synthetic point spread function of the UWB GPR. This point spread function is then used to be deconvolved from the recorded data. The method is evaluated on data coming from the UWB GPR and aspects like spatial resolution and the influence of the assumptions are discussed. Results of this migration method on cluttered data, obtained by the UWB GPR system during in- and out-door trials are found to be very good. Not only does the UWB GPR give enough depth resolution to distinguish the reflections on the targets from the air-ground reflections, but it has, after migration of the data, also enough resolution in the lateral

directions to give an idea of the shape and, in favorable circumstances, of the dimensions of the buried object.

REFERENCES

[1] L. Van Kempen, H. Sahli, J. Brooks and J. Cornelis, "New results on clutter reduction and parametric estimation for landmine detection using GPR," *Eight International Conference on Ground Penetrating Radar*, Gold Coast, Australia, pp. 872-879, May 2000.

[2] A. Pizurica, W. Philips, I. Lemahieu and M. Acheroy, "Speckle Noise Reduction in GPR Images," *Proc. of the International Symposium on Pattern Recognition, "In Memoriam Pierre Devijver"*, Brussels, Belgium, pp. 162-165, Feb. 1999.

[3] Y. Plasman, *Analyse en verwerking van sugnalen, komende van een ultra-wideband GPR*, Eindwerk, Royal Military Academy, Brussels, Belgium, 1999.

[4] B. Scheers, Y. Plasman, M. Piette, M. Acheroy and A. Vander Vorst , "Laboratory UWB GPR system for landmine detection," *Eight International Conference on Ground Penetrating Radar*, Gold Coast, Australia, pp. 747-752, May 2000.

[5] S. Mallat, *A wavelet tour of signal processing.* San Diego: Academic Press, 1998, ch. 1.

[6] S. R. Cloude, A. Milne, C. Thornhill and G. Crisp, "UWB SAR detection of dielectric targets," *IEE Eurel International Conference on The Detection of Abandoned Land Mines*, Edinburgh, UK, pp. 114-118, Oct. 1996.

[7] R. Prony, "Essai expérimental et analytique ... ", *L'Ecole Polytechnique*, Paris, vol. 1, no. 2, pp. 24-76, 1795.

[8] M. L. Van Blaricum and R. Mittra, "Problems and solutions associated with Prony's method for processing transient data," *IEEE Trans. on Antennas Propagat.*, vol. AP-26, no. 1, pp. 174-182, 1978.

[9] S. M. Kay, *Modern spectral estimation, theory and application*. New Jersey: Prentice-Hall Signal Processing Series, 1988, pp. 217-227.

[10] M. L. van Blaricum and R. Mittra, " A technique for extracting the poles and residues of a system directly from its transient response," *IEEE Trans. on Antennas Propagat.*, vol. AP-23, no. 6, pp. 777-781, Nov. 1975.

[11] R. Kumaresan and D. W. Tufts, "Improved spectral resolution III: Efficient realisation," *IEEE proceedings*, vol. 68, no. 10, pp. 1354-1355, Oct. 1980.

[12] D. W. Tufts and R. Kumaresan, "Estimation of frequencies of multiple sinusooids: Making linear prediction perform like maximum likelihood," *IEEE proceedings*, vol. 70, no. 9, pp. 975-989, Sep. 1982.

[13] M. A. Rahman and K. B. Yu, "Total least square approach for frequency estimation using linear prediction," *IEEE trans. Acoustic, Speech and Signal Processing*, vol. 35, pp. 1440-1454, Oct. 1987.

[14] C.-C. Chen and L. Peters, *Design and Development of Enhanced Ground Penetrating Radar Systems for the Detection and Classification of Unexploded Ordnances and Land Mines*, Joint Technical Report 733346-1, 733946-1, 730181-3, the Ohio State University, Ohio, USA, Sep. 1997.

[15] L. Carin, L. B. Felsen, D. R. Kraj, H. S. Oh, W. C. Lee and S. U. Pillai, "Wave-oriented signal processing of dispersive time-domain scattering data," *IEEE Trans. on Antennas Propagat.*, vol. AP-45, no. 4, pp. 592-600, April 1997.

[16] L. C. Trintinalia and H. Ling, "Feature extraction from electromagnetic backscattered data using joint time-frequency processing," *Ultra-Wideband, Short-Pulse Electromagnetics 3*. C. E. Baum, L. Carin and A. P. Stone, Eds., New York: Plenum Press, 1997, pp. 305-312.

[17] B. Scheers, M. Piette and A. Vander Vorst, "The detection of AP mines using UWB GPR," *IEE Second International Conference on The Detection of Abandoned Land Mines*, Edinburgh, UK, pp. 50-54, Oct. 1998.

[18] Ö. Yilmaz, *Seismic data processing*. Tulsa, USA: Society of Exploration Geophysicists, 1987.

[19] A. J. Berkhout, "Wave field extrapolation techniques in seismic migration, a tutorial," *Geophysics*, vol. 46, no. 12, pp. 1638-1656, Dec. 1981.

[20] M. Soumekh, *Synthetic aperture radar signal processing*. New York: John Wiley & sons, 1999.

[21] Egil Eide, *Radar imaging of small objects closely below the earth surface*, Doctoral thesis, Norwegian University of Science and Technology, Norway, Aug. 2000.

[22] R. H. Stolt, “Migration by Fourier Transform,” *Geophysics*, vol. 43, no. 1, pp. 23-48, Feb. 1978.

[23] H.C. Andrews and B.R. Hunt, *Digital Image Restoration*. New Jersey: Prentice Hall, 1977.

[24] J. van der Kruk, C. P. A. Wapenaar and J. T. Fokkema, “Multi-component 3-D imaging of ground penetrating radar data using matrix inversion in the spatial Fourier domain,” *Eight International Conference on Ground Penetrating Radar*, Gold Coast, Australia, pp. 508-513, May 2000.